Applied Catalysis B: Environmental 304 (2022) 121005

Contents lists available at ScienceDirect

Applied Catalysis B: Environmental

journal homepage: www.elsevier.com/locate/apcatb

Defect engineering technique for the fabrication of $LaCoO_3$ perovskite catalyst via urea treatment for total oxidation of propane

Chao Feng [a], Qianqian Gao [a], Gaoyan Xiong [a], Yanfei Chen [a], Yuan Pan [a,*], Zhaoyang Fei [b], Yanpeng Li [a], Yukun Lu [c], Chenguang Liu [a], Yunqi Liu [a,*]

[a] State Key Laboratory of Heavy Oil Processing, College of Chemical Engineering, China University of Petroleum (East China), Qingdao 266580, China
[b] State Key Laboratory of Materials-Oriented Chemical Engineering, Nanjing Technology University, Nanjing 211816, China
[c] College of Science, China University of Petroleum (East China), Qingdao 266580, China

ARTICLE INFO

Keywords:
Perovskite oxides
Defect engineering
Urea treatment
Propane oxidation
Oxygen species activation

ABSTRACT

The low defect content and poor oxygen mobility of perovskite catalysts limit its application in VOC elimination. Herein, we report a strategy involving defect engineering route following an easy urea treatment method to enhance the propane oxidation performance of perovskite catalysts. The constructed $LaCoO_3$-D43 exhibits superior catalytic activity (T_{90} = 309.3 °C), the T_{90} value is 150 °C lower than that of $LaCoO_3$, and excellent thermal stability against CO_2 and H_2O. Experimental results revealed that the urea pyrolysis resulted in the generation of La and O defects and rich surface-active Co species in high-valence states, increasing the utilization of Co active sites. DFT calculations show that the exposed Co surface is conducive to the adsorption and dissociation of oxygen and propane. This work provides a defect engineering strategy to effectively activate perovskite catalysts performance, and can be generalized for the fabrication of other types of perovskite catalysts.

1. Introduction

Volatile organic compounds (VOCs) are produced as the byproducts of the chemical and manufacturing industries. These compounds endanger the atmosphere and human health [1,2]. Propane is the most stable VOC [3]. The emission of propane is increasing day by day. This can be attributed to the increasing usage of liquefied petroleum gas (LPG) [4]. Therefore, an efficient and stable degradation technology should be developed to reduce the emission of propane gas. The catalytic oxidation technology is considered to be the most efficient method of reducing propane emissions. The method is highly efficient and requires the consumption of low amounts of energy [2]. The development and design of highly efficient catalyst is the principal problem and challenge confronted by this technology [5]. Thus, it is important to develop high-performance and highly stable catalysts for the efficient control of propane emissions.

Perovskite oxides have emerged as promising transition metal catalysts that can be used in various catalytic reactions as they are cost-effective, highly durable, and easy to synthesize. They are also characterized by variable chemical components [6]. Generally, the propane oxidation process on perovskite follows the Mars–van Krevelen (MvK) mechanism [7]. Perovskite oxide exhibits poor catalytic propane oxidation activity, which can be attributed to the inferior surface characterized by weak oxygen mobility [8]. Therefore, it can be inferred that the presence of oxygen defects could enhance the low-temperature performance. Various strategies as structural modification [3], usage of zeolite carriers [9,10], and element doping [11] have been used to achieve this. Zheng et al. [11] dispersed boron on $LaCoO_3$ crystals following the sol–gel method. This helped in the generation of crystal distortions and abundant oxygen defects. In sum, the traditional defect engineering strategy can be followed to adjust the crystal plane structure, causing lattice distortion. This can also be used to generate surface defects and oxygen vacancies. Compared to the traditional method, the surface modification defect engineering strategy gains an advantage to effectively regulate the nature and number of surface-active sites on perovskite [12,13]. Yang et al. [12] etched the surface of $La_{0.8}Sr_{0.2}CoO_3$ with dilute oxalic acid to increase the number of Co^{2+} Lewis acid sites and promote the activation of lattice oxygen and adsorbed oxygen species. This also helped enhance the extent of adsorption of propane. However, to date, the defect engineering method has only been used to modify the valence states of surface-active sites, adjust the number of acidic sites, and enhance the surface adsorption capacity. The method

* Corresponding authors.
E-mail addresses: panyuan@upc.edu.cn (Y. Pan), liuyq@upc.edu.cn (Y. Liu).

https://doi.org/10.1016/j.apcatb.2021.121005
Received 24 September 2021; Received in revised form 19 November 2021; Accepted 6 December 2021
Available online 9 December 2021

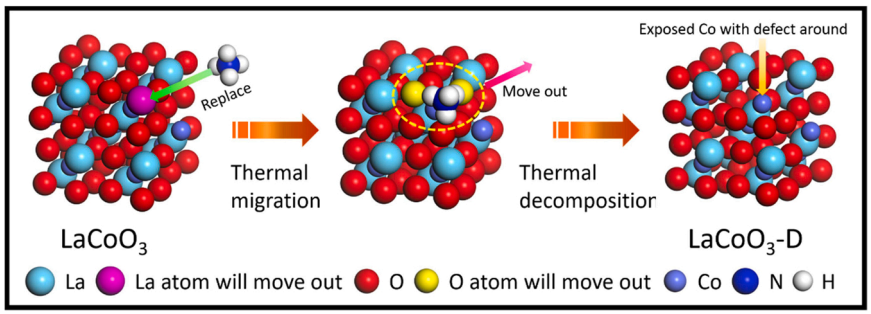

Scheme 1. Defect engineering route for the fabrication of the $LaCoO_3$-D catalyst.

could not be used to effectively create defects and improve the intrinsic activity of perovskite catalysts.

We modified the perovskite $LaCoO_3$ surface following a powerful defect engineering strategy that could be executed following a simple urea treatment method. The method could be used to enhance the propane oxidation activity. Results obtained from detailed experimental and theoretical characterization experiments suggest that, unlike the ordinary defect engineering method that can only be used to generate lattice distortions, the presented method (executed following the urea treatment method) can be used to fabricate $LaCoO_3$ with large numbers of La defects. The surface-active Co species in their high-valence states could also be exposed efficiently. Simultaneously, the defect engineering process helps in the generation of a large number of oxygen defects and active oxygen species on the surface. This promotes the process of reactant adsorption and dissociation. Thus, it helps to improve the utilization of the Co active sites for improving the catalytic propane oxidation performance. This work reports a defect engineering mechanism that can be used to effectively activate and improve the performance of perovskite catalysts. The process can be generalized to develop other types of perovskite catalysts.

2. Experimental

2.1. Catalyst preparation

2.1.1. Synthesis of $LaCoO_3$

$LaCoO_3$ was synthesized following a sol–gel method [14]. The same amounts of cobalt nitrate (Aladdin, ≥ 99%) and lanthanum nitrite (Sinopharm chemical reagent, ≥ 99%) were dissolved in 50 mL of deionized water to form a clear solution. Following this, citric acid (Sinopharm chemical reagent, ≥ 99.5%) was added dropwise to the prepared solution under conditions of vigorous stirring. The mixture was stirred for 1 h at 50 °C. Following this, it was centrifuged and dried at 80 °C over 12 h. The prepared catalyst was calcined in air at 600 °C for 6 h.

2.1.2. Synthesis of $LaCoO_3$ with defect ($LaCoO_3$-D)

The prepared $LaCoO_3$ and urea were mixed under the mass ratios of 1:X (X = 0.2, 0.7, 1, 1.5, and 2.0). The mixture was ground to form a uniform powder. The samples were then calcined in a muffle furnace at 650 °C for 1 h. The black powders were collected, washed, and dried. The sample was labeled $LaCoO_3$-DR, where R is the surface defect content in percent calculated using the X-ray photoelectron spectroscopy (XPS) technique. When (La + O)/Co of $LaCoO_3$ is considered the zero point, R denotes the (La + O)/Co ratio in $LaCoO_3$-D and $LaCoO_3$. The relevant data are listed in Table S1.

2.2. Catalyst characterization

Data obtained using the X-ray diffraction (XRD), Raman spectroscopy, scanning electron microscopy (SEM), transmission electron microscopy (TEM), high-resolution transmission electron microscopy (HRTEM), energy-dispersive X-ray spectroscopy, (EDS) elemental mapping, inductively coupled plasma (ICP), Co K-edge X-ray absorption fine structure (XAFS) spectroscopy, XPS, Fourier transform infrared (FT-IR) spectroscopy, electron paramagnetic resonance (EPR) spectroscopy techniques are presented in the Supporting information (SI). The nitrogen adsorption–desorption isotherms, H_2 temperature-programmed reduction (H_2-TPR), and O_2 temperature-programmed desorption (O_2-TPD) curves are also presented in the SI.

2.3. Determination of catalytic activity

The catalytic activity of the catalyst in total propane oxidation was tested using a U-shape bed quartz tube reactor (inner diameter = 6 mm) in the presence of 200 mg of the catalyst (40–60 mesh). The activity was determined in the temperature range of 150–475 °C. The flow of the feed gas mixture was set at 100 mL min^{-1} (GHSV = 30,000 h^{-1}). It consisted of 2500 ppm of C_3H_8 and air as the balance gas. The reaction products were monitored and analyzed online using a Fuli instrument (GC-9720 gas chromatograph) equipped with a flame ionization detector for VOCs detection. Data on the reaction kinetics are shown in the SI.

2.4. Calculation details

All calculations were performed using the density functional theory (DFT) technique using the Vienna ab initio simulation package (VASP) [15]. Spin-polarized calculations were performed using the generalized gradient approximation (GGA) combined with the Perdew–Burke–Ernzerhof (PBE) method to determine the exchange and correlation energies. The projector-augmented wave (PAW)[16] method was used to represent the core–valence electron interactions. The typical plane-wave cutoff energy was 400 eV for basis-set expansion. For geometry optimization calculations, forces were converged below 0.03 eV $Å^{-1}$. The SCF convergence energy was 1×10^{-5} Ha[17]. A $1 \times 1 \times 1$ k-point mesh was used to perform all the calculations. The definition and calculation details for oxygen vacancy formation energy and the Gibbs free energy are presented in SI.

3. Results and discussion

3.1. Textural characteristics

$LaCoO_3$-D catalysts were fabricated following a defect engineering strategy, as shown in Scheme 1. NH_4^+ generated during the pyrolysis of urea can displace La^{3+} as they are similar in size [18]. They also exhibit weak interactions toward the face of the CoO_6 octahedra and form an N-H-O-Co staggered conformation [19]. N-H moves out of the crystal phase, resulting in the generation of La and O defects in the crystalline lattice when urea is further pyrolyzed [20]. With an increase in the urea treatment capacity, the defect content on the surface increases from 26% (treatment capacity: 0.2 times) to 43% (treatment capacity: 1.5 times). However, a further increase in the urea treatment capacity (by 2 times) resulted in a significant drop in the defect content to 18%.

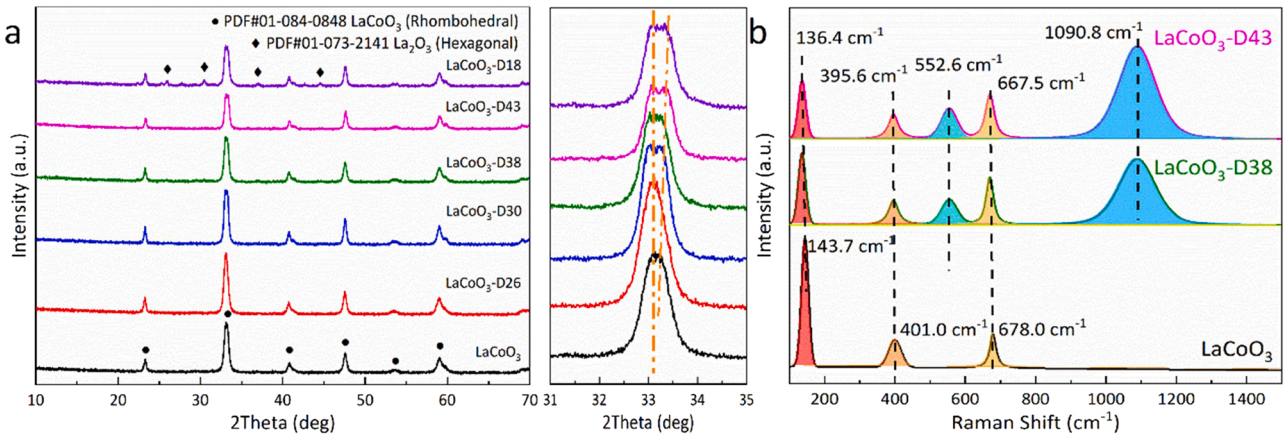

Fig. 1. (a) Powder XRD patterns, (b) Raman spectra profiles of the $LaCoO_3$-D catalysts.

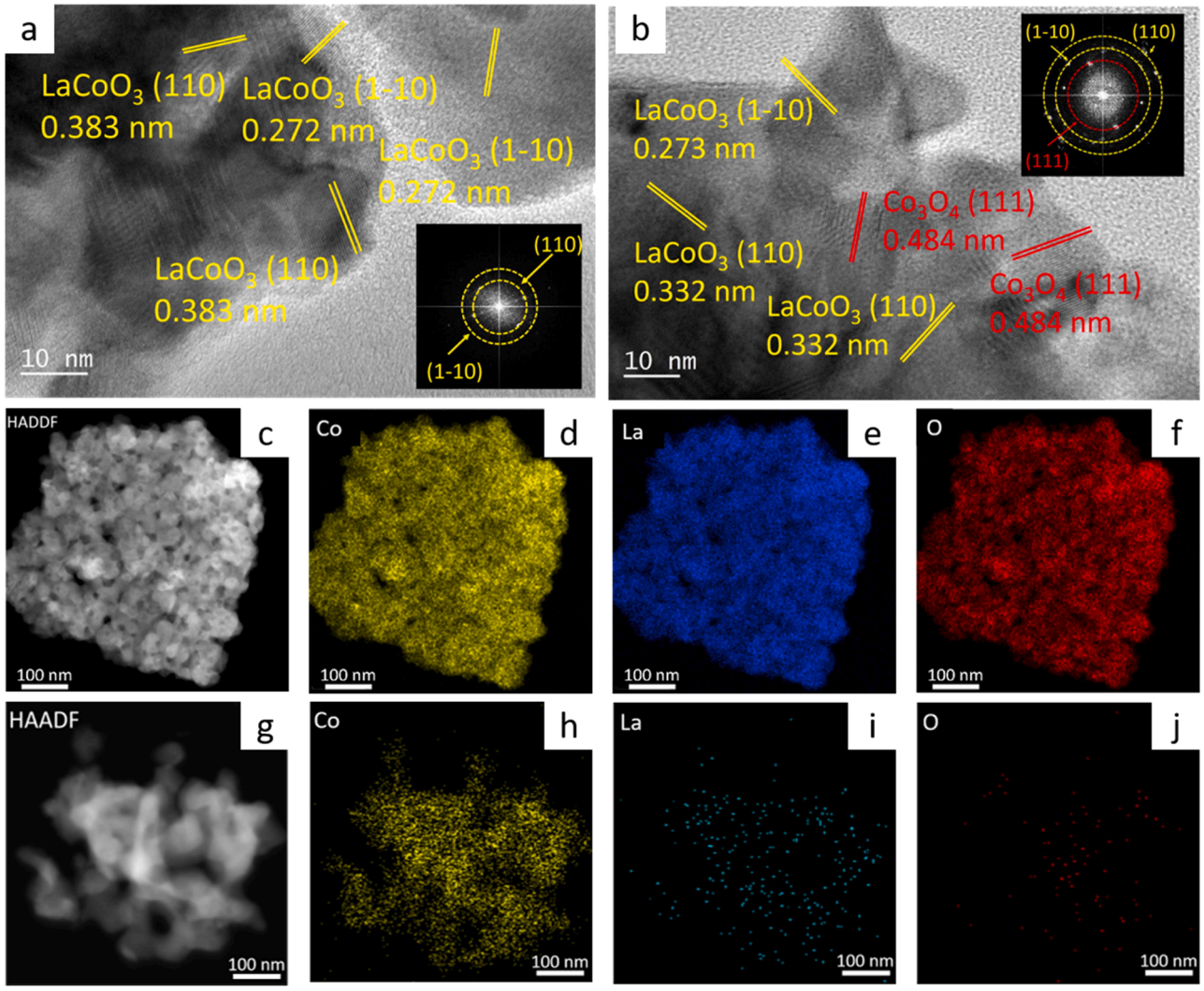

Fig. 2. HRTEM images of (a) $LaCoO_3$ and (b) $LaCoO_3$-D43, and elemental mapping of (c–f) $LaCoO_3$ and (g–j) $LaCoO_3$-D43.

The crystal structure of the $LaCoO_3$-D catalysts treated following the defect engineering method was analyzed using the XRD technique. The main peaks of all the as-synthesized catalysts are indexed to the pure $LaCoO_3$ rhombohedral crystalline phases (PDF#84-0848) [14] (Fig. 1**a**). An increase in the urea treatment capacity resulted in a decrease in the intensity of the diffraction peaks. The peaks at 33.3° shifted to a high angle, indicating that lattice distortion occurred on the surface of the perovskite [21], resulting in a reduction in the crystal sizes from 40.06 to 31.51 nm (Table S2). Additionally, the generation of new weak peaks corresponding to La_2O_3 (PDF#73-2141) was observed in the patterns recorded for $LaCoO_3$-D18. The decrease in the surface defect content can be attributed to the formation of La_2O_3 impurity. The Raman spectral

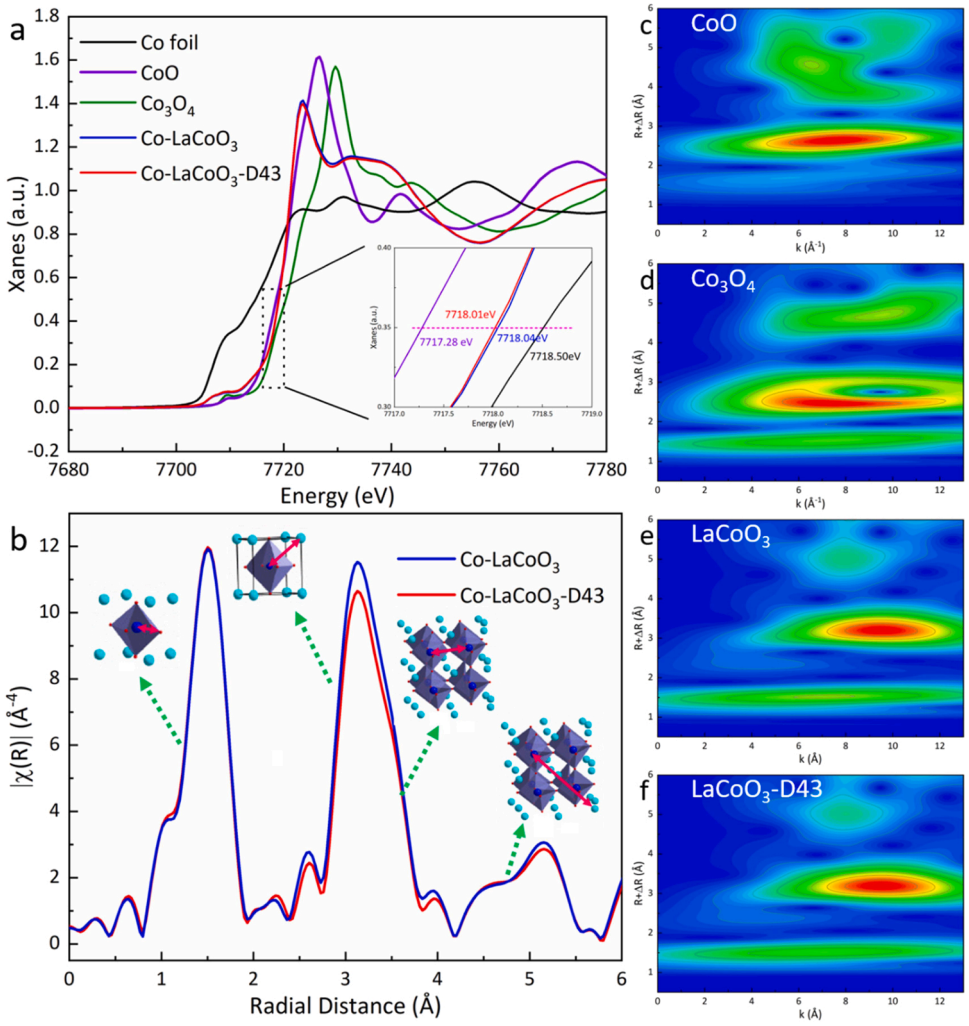

Fig. 3. (a) Co K-edge XANES, (b) the R-space Fourier-transformed FT (k3 χ(k)) of Co K-edge EXAFS profiles recorded for $LaCoO_3$ and $LaCoO_3$-D43 catalysts. WT plots at the Co Kedge of (c) CoO, (d) Co_3O_4 (e) $LaCoO_3$, and (f) $LaCoO_3$-D43.

profile recorded for $LaCoO_3$ (Fig. 1**b**) exhibited three peaks at 143.7 cm^{-1}, 395.6 cm^{-1}, and 667.5 cm^{-1}. They are characteristic peaks of $LaCoO_3$ [22]. Analysis of the Raman spectral profiles recorded for $LaCoO_3$-D38 and D43 revealed that the vibration of La became weaker, while that of CoO_6 became stronger [23]. Two additional peaks appeared at 552.6 cm^{-1} and 1090.8 cm^{-1} appeared. These were assigned to the stretching mode of Co-O-Co and the symmetric stretching mode of the double bond in the terminal Co═O group present in the highly distorted CoO_6 structure, respectively[24].

The morphological features of the $LaCoO_3$-D materials were studied using the SEM and TEM techniques. $LaCoO_3$-D catalysts exhibited a block structure with lamellar surface structure (Fig. S1) composed of random aggregations of uniform nanoparticles (grain size: 18–20 nm; Fig. S2). An increase in the urea treatment capacity resulted in an increase in the size of the perovskite block. Under these conditions, the layer became smoother. This could be attributed to the bonding effect generated under conditions of urea addition. The N_2 adsorption-desorption experiments revealed that all the $LaCoO_3$-D catalysts displayed mesoporous structures [25] (Fig. S3). The $LaCoO_3$-D catalysts also exhibited larger BET surface area, total pore volume and pore size after urea treatment (Table S3). HRTEM images of $LaCoO_3$ revealed that the interplanar spacing was 0.272 nm and 0.383 nm, corresponding to the (1–10) and (110) faces of the $LaCoO_3$ crystal phase, respectively (Fig. 2**a**). A new lattice spacing of 0.484 nm appeared in the HRTEM image recorded for $LaCoO_3$-D43 (Fig. 2**b**). The value was close to the value recorded for the Co_3O_4 (111) face (PDF#76-1802; 0.466 nm), implying that the process of defect engineering could be used to form a surface characterized by the presence of Co-O coordination at the edges [26]. Analysis of the EDS elemental mapping images reveals that Co, La, and O are distributed uniformly on the $LaCoO_3$ cluster (Fig. 2**c–f**). Moreover, we analyze composition and the amount of $LaCoO_3$ and $LaCoO_3$-D43 via EDS, ICP and XPS (Table S4). The results reveal that following urea treatment, the number of La and O on the $LaCoO_3$-D43 surface decreased significantly (Fig. 2**g–j**).

XAFS is an efficient technique that can be used to analyze the electronic structure as it helps achieve high spatial resolution. The adsorption edge position observed in the X-ray absorption near edge structure (XANES) spectral profiles of $LaCoO_3$ and $LaCoO_3$-D43 is located between that of CoO and Co_3O_4 (Fig. 3**a**), demonstrating that the Co species in $LaCoO_3$ and $LaCoO_3$-D43 carry a positive charge between + 2 and + 3 [27]. The almost identical absorption edges structures of $LaCoO_3$ and $LaCoO_3$-D43 indicate that the oxidation states of the Co ions present in both the samples are close to each other. This signifies that chemical etching (of La segregation) exerts little effect on the perovskite structure, especially the Co structure [20]. The R-space Fourier-transformed FT ($k^3\chi(k)$) of the Co K-edge extended X-ray absorption fine structure (EXAFS) profiles recorded for $LaCoO_3$ and $LaCoO_3$-D43 presents three dominant shells (located at ~ 1.53 Å, ~ 3.14 Å, and ~ 4.83 Å) (Fig. 3**b**). These can be attributed to the Co—O bond, Co—La(Co) bond, and Co—La(Co)—O bond present in the corner-sharing octahedra,

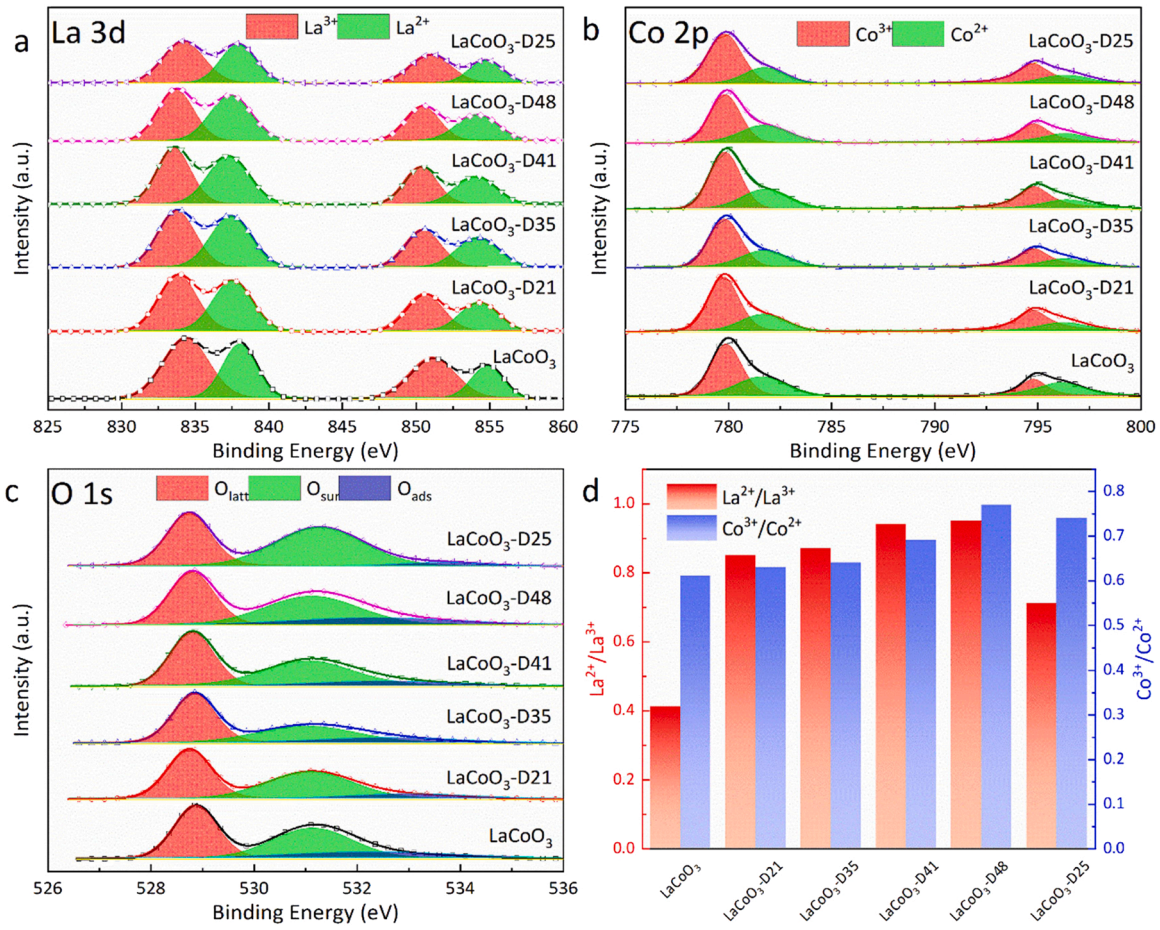

Fig. 4. (a) La 2p, (b) Co 2p, (c) O 1s, (d) La^{2+}/La^{3+}, and Co^{3+}/Co^{2+} molar ratios for the synthesized $LaCoO_3$-D catalysts before reaction.

respectively [28]. The peak positions and intensities of the Co—O bond present in $LaCoO_3$ and $LaCoO_3$-D43 do not change, and the coordination number and bond length of the Co—O bond were identical before and after urea treatment [29]. The results indicate that the process of defect engineering would not affect the coordination of the Co-O basic unit, and the possibility of Co—N bonding on the surface could be excluded. The peak positions of the Co-La shell for $LaCoO_3$ and $LaCoO_3$-D43 remained the same, but the peak intensity decreased following urea treatment. This indicated that the amount of Co-La coordination was reduced. But the coordination state of Co-Co remained the same. Similar coordination states were observed in the third shell of the Co-La(Co)-O coordination. Comparing the coordination states of Co-La and Co-Co, the urea-etched surface plays a crucial role during the formation of the corner-sharing octahedra bearing La defects. A decrease in the extent of La segregation could slightly increase the extent of charge transfer and increase the number of active sites [30]. The wavelet transform plots (Fig. 3**c–f**) generated for $LaCoO_3$ and $LaCoO_3$-D43 show a maximum at k = 7.1 Å (R = 1.5 Å) and k = 9.5 Å (R = 3.1 Å). These corresponded to the scattering of Co-O and Co-La(Co) in the $LaCoO_3$ perovskite.

3.2. Analysis of the surface chemical properties

The surface elemental composition and chemical states of the $LaCoO_3$-D catalysts were investigated using the XPS technique. The Co/(Co + La) ratio on the surface increased from 0.25 to ~ 0.38 with the formation of defects (Table S5). The XPS La 3d spectra displayed two major peaks at approximately 835 eV and 853 eV (Fig. 4**a**), which can be attributed to the typical La $3d_{5/2}$ and La $3d_{3/2}$ orbitals [31]. The La^{2+}/La^{3+} ratios follow the order $LaCoO_3$-D43 > $LaCoO_3$-D38 > $LaCoO_3$-D30 > $LaCoO_3$-D26 > $LaCoO_3$-D18 > $LaCoO_3$ (Fig. 4**d**). A higher La^{2+} ratio, signifying a decrease in the coordination number and valence state of La, indicates an increase in the oxygen vacancies on the surface results in an increase in the ability to transfer surface active oxygen species [32]. The Co 2p spectra could be deconvoluted into Co^{3+} and Co^{2+} spin doublets at 779 eV, 794 eV and 781 eV, and 796 eV (Fig. 4**b**) [33]. The content of the Co^{3+} species on the surface increase with an increase in the defect content (Fig. 4**d**). As the Co^{3+} species function as the active sites during the catalytic reactions, high Co^{3+}/Co^{2+} ratios can improve the activation and migration of the oxygen species, which promotes the adsorption and dissociation of the C—H bonds [12,34]. The O 1s spectra were decomposed into three components: lattice oxygen (O_{latt}, 529.5 eV), surface adsorbed oxygen (O_{sur}, 531.5 eV), and physically adsorbed oxygen (O_{ads}, 533.5 eV) (Fig. 4**c**) [35]. The $LaCoO_3$-D sample contained abundant O_{sur} + O_{ads}%, which can be attributed to the formation of the surface La and O defects. Additionally, the $LaCoO_3$-D43 sample possessed the highest density of oxygen dissociation sites, revealing excellent activity and interactions with reactants [36].

FT-IR spectra are recorded to analyze the surface chemical bond states. All $LaCoO_3$-D catalysts present similar FT-IR spectral profiles with three absorption peaks around 426 cm^{-1}, 594 cm^{-1}, and 674 cm^{-1} (Fig. 5**a**). These can be attributed to the stretching vibration of Co-$O_{(I)}$ (E_u vibration mode), stretching vibration of the La—$O_{(II)}$—Co bond (A_{2u} vibration mode), and bending vibration of Co-$O_{(I)}$ ($\delta_{O\text{-}Co\text{-}O}$), respectively [37]. A blue shift in the peak positions is observed with an increase in the defect content, indicating that the force constants (*k*) for the Co—O and La—O—Co bonds (calculated following Hooke's law) gradually decreased [38]. The $LaCoO_3$-D43 catalyst was characterized by the minimum *k* value, indicating that the surface lattice distortion made the

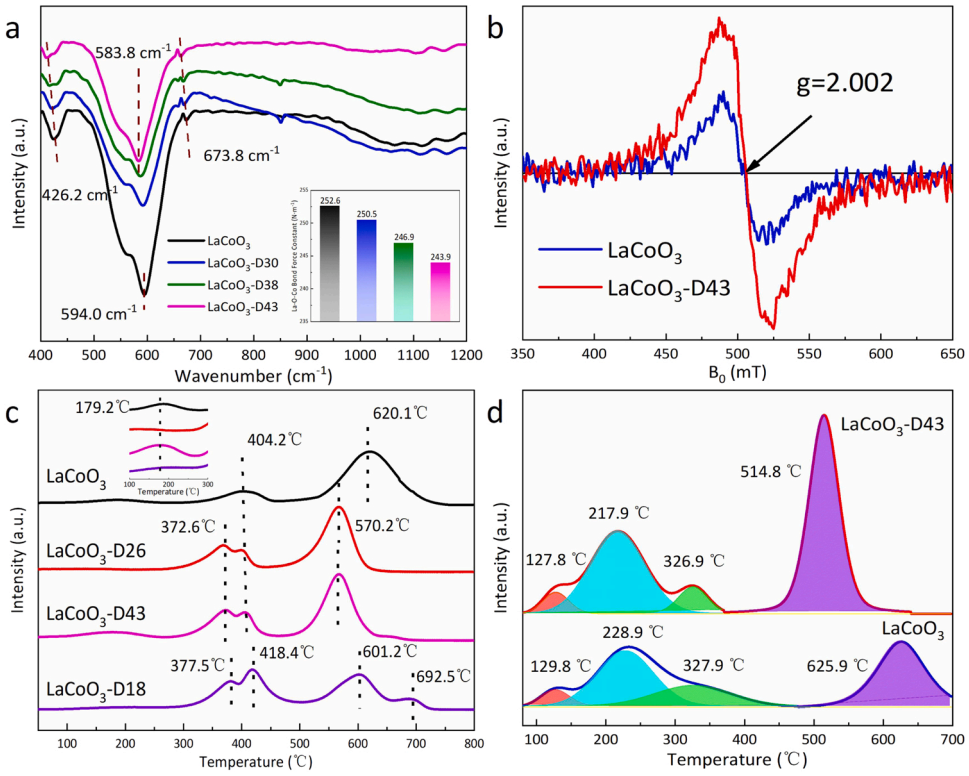

Fig. 5. (a) FT-IR spectral profiles and the calculated force constants for the La—O—Co bond (following Hooke's Law (inset)), (b) EPR spectral profiles, (c) H_2-TPR curves, and (d) O_2-TPD profiles recorded for the $LaCoO_3$-D catalysts.

vibration intensity weaker, resulting in better surface oxygen migration.

The surface defect state was further determined using the EPR technique. The EPR spectral profile recorded for $LaCoO_3$-D43 exhibited a notable axial sign around $g_{av} = 2.003$ (Fig. 5**b**), which was attributed to the superoxide anion (O^{2-}) signal [39]. It indicates that the number of surface oxygen defects increased significantly following defect engineering treatment. This is conducive to the enhancement of the Co active site's ability to activate oxygen species.

H_2-TPR experiments were conducted to investigate the reducibility of the $LaCoO_3$-D samples and determine the catalytic activity of the adsorbed oxygen on the surface. A quite weak signal is detected at 100–300 ℃, which attributed to the reduction of adsorbed oxygen species. Two reduction peaks appeared at approximately 405 °C and 616 °C in the H_2-TPR profile of the $LaCoO_3$ sample (Fig. 5**c**). The peaks reflected the reduction of Co^{3+} to Co^{2+} and Co^{2+} to Co^0 [40], respectively. Following urea treatment, the peak at approximately 400 °C split into an additional peak that appeared in the lower temperature region, attributable to the stronger reduction performance of Co^{3+} with defect around. $LaCoO_3$-D43 exhibits the maximum H_2 consumption ability below 400 °C. This can be attributed to the fact that the generation of defects resulted in the cleavage of the La-O bond and weakening of the Co—O bond present on the surface (Table S6).

O_2-TPD profiles were recorded to further analyze the properties of the surface oxygen species. $LaCoO_3$-D43 exhibited a similar distribution pattern for the processes of physical and chemical oxygen adsorption [41] on the surface in the temperature range of 100–400 °C, as $LaCoO_3$ (Fig. 5**d**). However, $LaCoO_3$-D43 is characterized by an intense peak corresponding to lattice oxygen desorption. A significant shift in the lower temperature range was observed (Table S7), demonstrating that the lattice oxygen transferability of the surface increases following the process of urea treatment.

3.3. *Catalytic performance and kinetic parameters for propane oxidation*

As the primary products formed during all the reaction processes were H_2O and CO_2, the $LaCoO_3$-D catalysts exhibited excellent selectivity for the total oxidation of propane. Based on the T_{90} temperature, it can be inferred that the activities follow the order of $LaCoO_3$-D43 > $LaCoO_3$-D38 > $LaCoO_3$-D30 > $LaCoO_3$-D18 > $LaCoO_3$-D26 > $LaCoO_3$. (Fig. 6**a**). 90% propane conversion using the $LaCoO_3$-D43 catalyst was achieved at 309.3 °C, a temperature that is almost 150 °C lower than that of $LaCoO_3$ (T_{90} = 460.9 °C). The propane consumption rate achieved in the presence of $LaCoO_3$-D43 at 220 °C is 9.32×10^{-6} mol g_{cat}^{-1} s^{-1} (Table 1). This value is five times higher than that recorded for the $LaCoO_3$ catalyst. The $LaCoO_3$-D43 catalyst exhibits a high specific surface activity (Fig. 6**b**) and TOF (Fig. 6**c**) for propane oxidation. The apparent activation energy (E_a) was determined by analyzing the linear Arrhenius plot (Fig. 6**d**). It was observed that the $LaCoO_3$-D43 catalyst exhibited the minimum E_a (38.99 kJ mol^{-1}) for propane oxidation. Compared to other previously reported catalysts (Table S8), $LaCoO_3$-D43 exhibits better catalytic performance, illustrating the fact that defect engineering by urea treatment is a promising modification method that can be used for the fabrication of oxidation catalysts.

The number of Co reaction sites on the surface, the extent of reducibility, and the number of oxygen species can potentially be the vital features that dominate the catalytic performance as the systems exhibit similar textural properties. The increased extent of surface-active Co exposure (Fig. 6**e**) induced by defect engineering increases the number of reaction sites for reactant adsorption and activation. However, the reduction in the extent of utilization of Co on the surface of $LaCoO_3$-D18 (attributable to the generated small particles of La_2O_3) results in decreased oxidation activity. The defect engineering technique can be used to increase the Co^{3+} content on the surface, resulting in increased acidity and reduction performance of the surface [11]. It was conducive to the initial step of the propane oxidation process. In

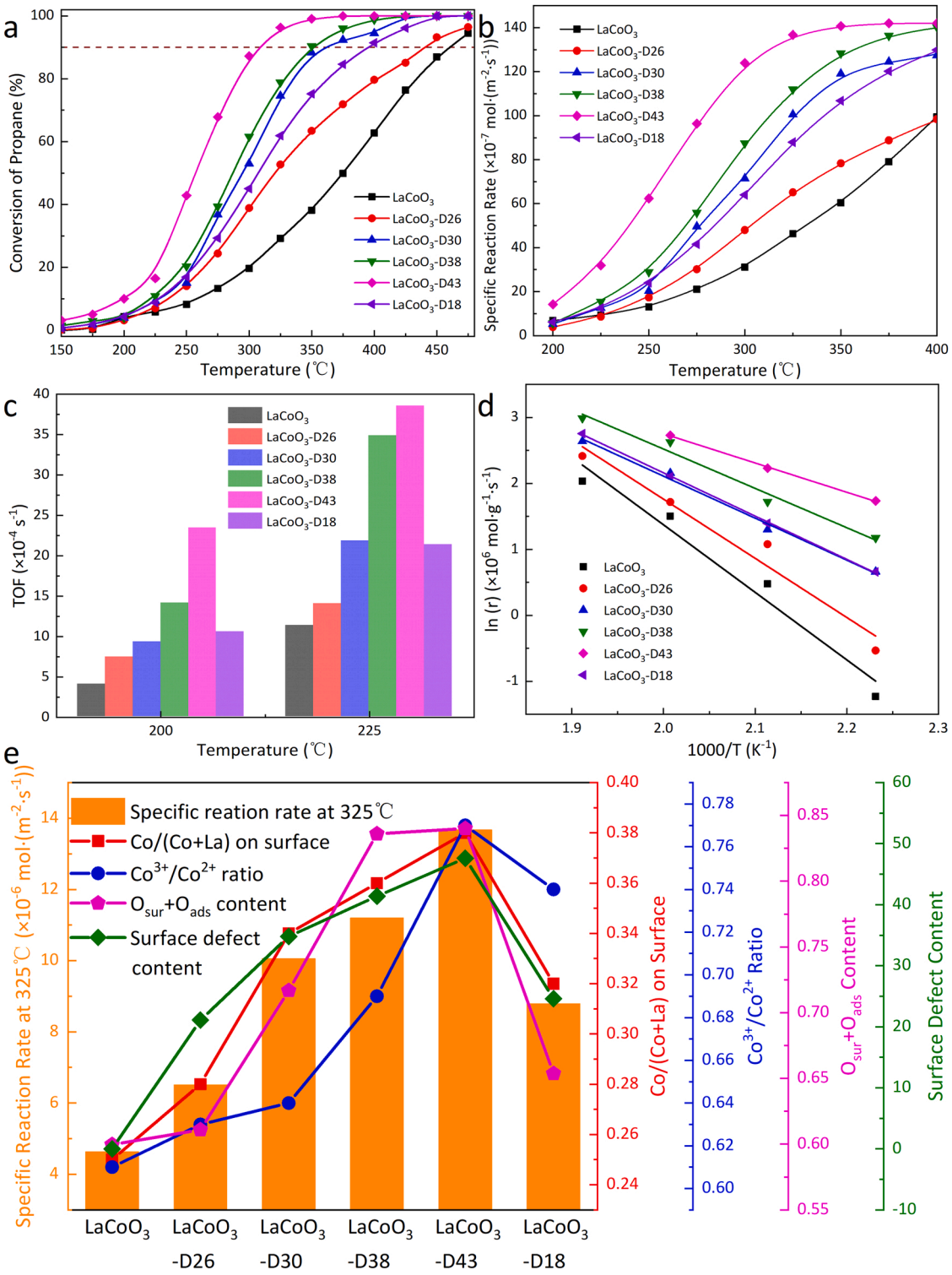

Fig. 6. (a) Propane conversion, (b) specific surface activity, and (c) TOFs recorded for the process of propane oxidation in the presence of $LaCoO_3$-D catalysts (reaction conditions: 200 mg of catalyst, 2500 ppm of C_3H_8 and balance Air, 30,000 h^{-1}). (d) Arrhenius plots. (e) Correlation between the specific surface activity at 325 °C and the ratios of the surface species recorded for the $LaCoO_3$-D catalysts.

addition, surface oxygen species were also influenced by the defect engineering method. The improvement in the lattice oxygen mobility was confirmed by analyzing the O_2-TPD profile. This helped enhance the propane catalytic oxidation performance achieved following the MvK mechanism. Secondly, the large number of surface oxygen vacancies (determined using the EPR technique) generated following the process of defect engineering boosted the adsorption capacity of the oxygen molecules present near Co. The reversible process Co^{2+}-□-Co^{2+} + O_2 ↔ Co^{2+}-□-Co^{3+}-O_2 ↔ O^--Co^{3+}-□-Co^{3+} + O^- could proceed readily [42]. After O^- (and O_2^-) activated, because of it is electrophilic, it can abstract H atom from adsorbed propane to form alkyl radicals, which can undergo deep oxidation at a lower temperature, resulting in a significant increase in the propane oxidation activity.

During the process of propane oxidation reaction, $LaCoO_3$-D

Table 1
Catalytic activities (T_{10}, T_{50}, T_{90}), reaction rates (r, at 220 °C), specific surface activity (SSA, at 220 °C), activation energies (E_a), and TOF (at 220 °C), recorded for the $LaCoO_3$-D catalysts.

Sample	T_{10} °C	T_{50} °C	T_{90} °C	$R_{220} \times 10^{-6}$ (mol $(g_{cat}\ s)^{-1}$)	SSA $\times 10^{-7}$ (mol $(g_{cat}\ s)^{-1}$)	E_a (kJ mol^{-1})	TOF $\times 10^{-4}$ (s^{-1})
$LaCoO_3$	258.2	375.1	460.9	1.61	2.74	57.73	4.04
$LaCoO_3$-D26	237.0	320.7	440.9	2.94	3.90	51.77	7.40
$LaCoO_3$-D30	226.7	295.1	364.1	3.67	5.32	50.91	9.26
$LaCoO_3$-D38	220.2	287.0	352.1	5.59	8.53	47.04	14.09
$LaCoO_3$-D43	199.8	256.4	309.3	9.32	14.23	38.99	23.45
$LaCoO_3$-D18	227.8	307.1	396.3	4.04	6.16	53.32	10.51

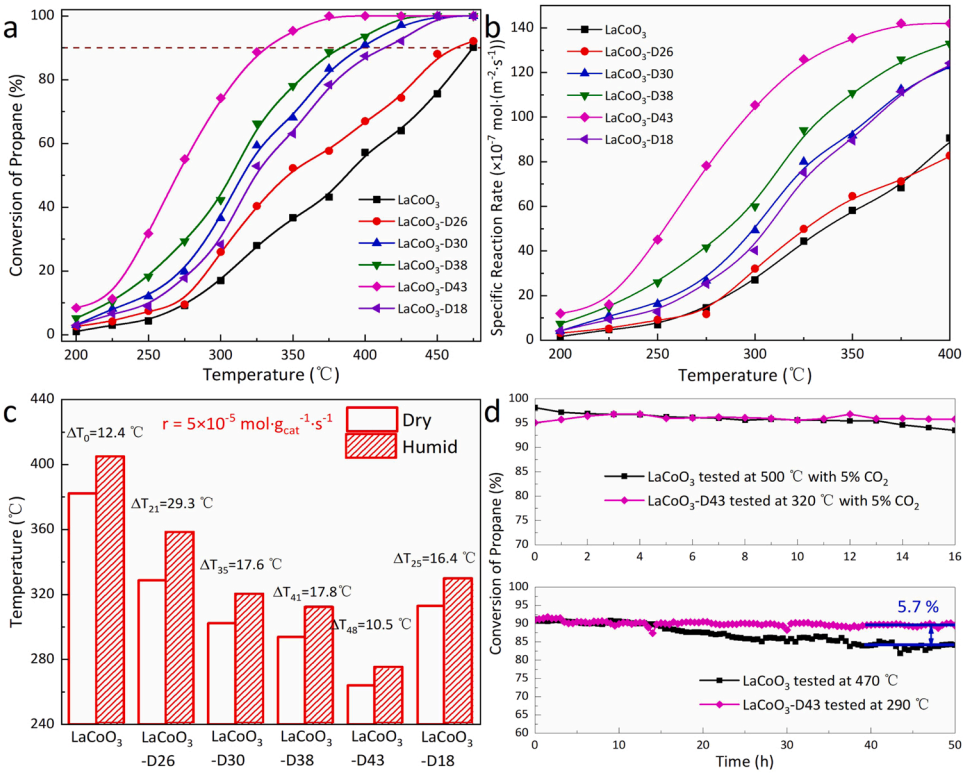

Fig. 7. (a) Propane conversion, (b) specific surface activity of propane oxidation over the $LaCoO_3$-D catalysts under humid conditions (reaction conditions: 200 mg of catalyst, 5 vol% of H_2O, 2500 ppm of C_3H_8 and balance air, at 30,000 h^{-1}). (c) Comparison of reaction temperature for the $LaCoO_3$-D catalysts at the reaction rate of 5×10^{-5} mol g_{cat}^{-1} s^{-1} under dry and humid conditions. (d) Long-term stability of the $LaCoO_3$-D catalysts used for propane oxidation under conditions of dry air and CO_2.

catalysts exhibited high structural stability. The XRD patterns recorded for $LaCoO_3$-D43 retained the perovskite structure following the reaction (Fig. S4). $LaCoO_3$-D43 exhibited a nanoparticle structure. The particles possessed the same crystal plane as before (Fig. S5). This indicated that the crystal structure remained unchanged. Meanwhile, the content of La and Co did not change significantly following the reaction (Fig. S6, Table S9**)**. This indicated that the surface elemental structure was quite stable.

To explore the influence of water vapor, 5 vol% of H_2O was added to the feed gas. The curves corresponding to the process of propane conversion under humid conditions shifted to a higher temperature (Fig. 7**a**) region, signifying a negative influence on catalytic activities. Nevertheless, $LaCoO_3$-D43 still exhibited the maximum catalytic performance among all the $LaCoO_3$-D catalysts (based on the lowest T_{90} value (T_{90} = 329.4 °C)) and the maximum SSA (in terms of the defined temperature) (Fig. 7**b**). To attain the same reaction rate (5×10^{-5} mol g_{cat}^{-1} s^{-1}; as that achieved under dry conditions), the reaction temperature of the $LaCoO_3$-D43 catalyst under humid conditions should be increased by only 10.5 °C (Fig. 7**c**). Besides resistance to water vapor, the $LaCoO_3$-D43 catalyst exhibits excellent stability over a 16 h long reaction with the introduction of 5% CO_2 (Fig. 7**d**). It also exhibits excellent cyclic stability (Fig. S7) and better long-term stability than $LaCoO_3$ (Fig. 7**d**).

3.4. Density function theory calculation

The electronic structure of $LaCoO_3$ containing La and O defects was further assessed to gain insight into the influence of the defect engineering process on the structure of perovskite. Analysis of the charge density difference plot reveals that electron vacancies are formed at the La and O defects present on the surface. This attracts guest molecules that can be adsorbed at the defect sites (Fig. 8**a**) [43]. It was observed that the charge density of the exposed Co atomic surface increased (Fig. 8**b**). This improves the electron transfer efficiency of the reaction. The electron region distribution before and after defect engineering treatment was compared. An increase in the electron density around Co following the formation of defects was observed (Fig. 8**c,d**). Analysis of the density of states (DOS) plots (Fig. 8**c,d**) confirms that in the presence of defects, the DOS peak of $LaCoO_3$-D ($E_{P\text{-}LaCoO3\text{-}D}$ = 0.38 eV) is closer to the Fermi level (E_F) (Fig. 8**e ,f**). This indicates a high electron conduction efficiency between the substrates and intermediates [44,45]. The increase in the projected density of states of Co and O near E_F helps improve electrical conductivity, rate of electron transport, and extent of ion diffusion on the surface [46].

The oxygen vacancy formation energy, E_v, is used as a predictor of the oxidation reaction capacity of the catalyst [47]. The Co-layer on the $LaCoO_3$-D surface, formed following the defect engineering technique, was characterized by a low oxygen vacancy formation energy (E_v

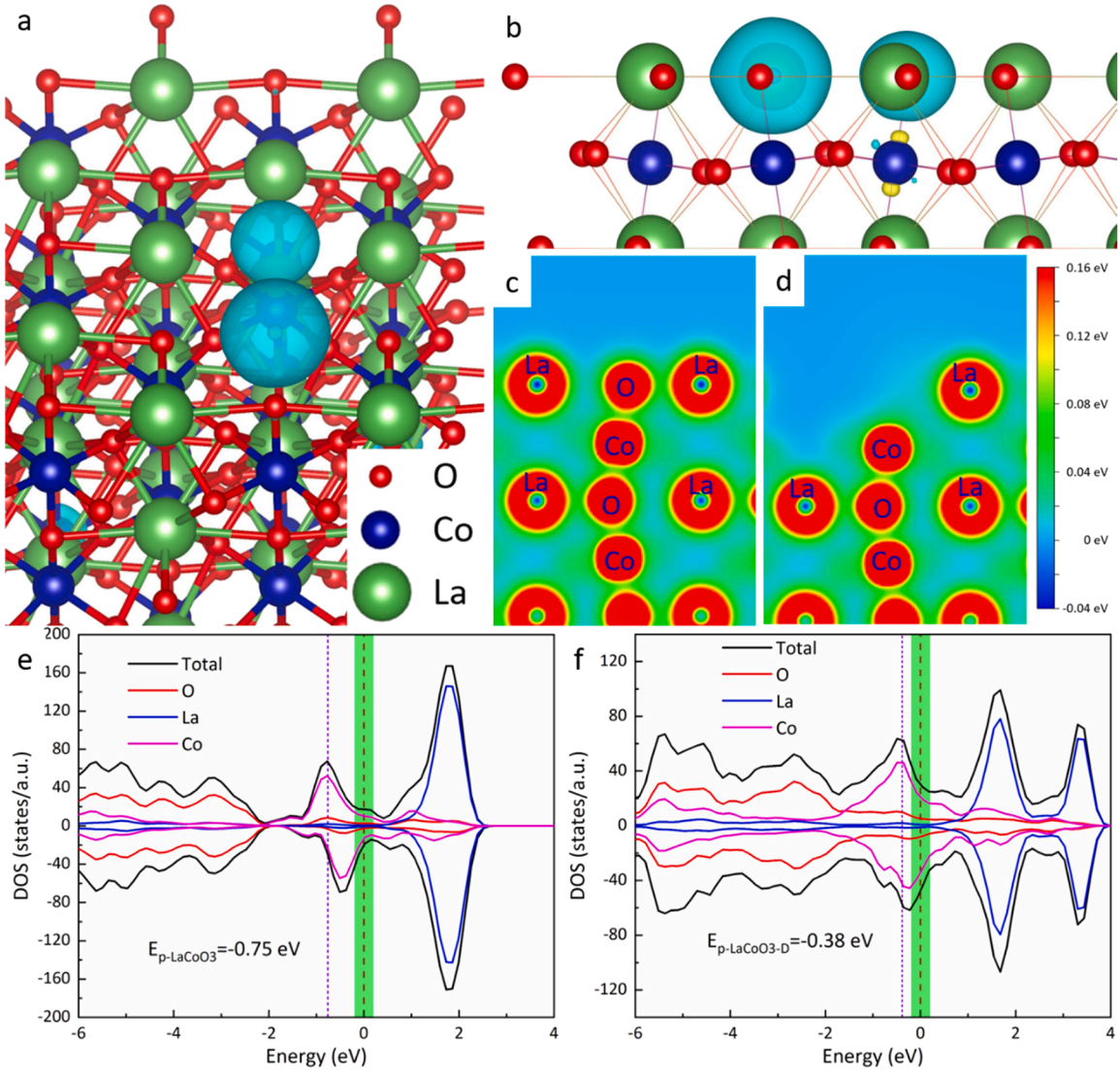

Fig. 8. Charge density difference plot generated for La and O defects on the surface of $LaCoO_3$. View from (a) above and (b) side. The isosurface value is 0.002 e $bohr^{-3}$. The yellow and blue isosurfaces represent positive and negative charges, respectively. Electron location function of (c) $LaCoO_3$ and (d) $LaCoO_3$ with La and O defects. Calculated DOSs for (e) $LaCoO_3$ and (f) $LaCoO_3$ with La and O defects.

= 1.01 eV) (Fig. 9**a**). This indicated that oxygen vacancies are easier to form on surface after urea treatment. Following the adsorption of the oxygen gas on the vacancy sites, one O atom of O_2 recovers the lattice oxygen, while the other O atom becomes the active oxygen species [48]. Results obtained using the DFT technique (Fig. 9**b**) indicate that the O atom desorption energies (on the exposed Co surface; 0.36 eV) are low. The value reflects the order of catalytic performance, indicating that oxygen can be effectively activated on the reduced surfaces of $LaCoO_3$-D. Systematic DFT calculations have been conducted to analyze the initial steps of propane combustion, that adsorption of propane and dissociation of the C—H bonds [3,49]. Fig. S8 displayed the adsorption structures of propane. The C—H bond of secondary carbon was adsorbed on O site of La-layer and Co-layer. The adsorption energies of propane recorded for the Co-layer and La-layer were 0.14 eV and 0.25 eV (Fig. 9**c**), respectively. This indicated that propane could be weakly adsorbed on the surface. After adsorption, the C—C and C—H bond lengths change in varying degrees. Propane adsorbed on Co-layer exhibited a longer C—H (1.128 Å) and C—C (1.538 Å) bond lengths (Table S10), signifying that propane can be effectively activated on Co-layer. The reaction energy profile of propane reaction with lattice oxygen via the MvK mechanism is illustrated in Fig. 9**d** [7,42]. The propane dissociation energy on the Co surface (0.72 eV) is much lower than that on the La surface (1.37 eV), indicating that the C—H bond could readily react with the Co-O resulting in dissociation. These strong evidences reveal that the $LaCoO_3$-D structure containing exposed Co units can promote the activity of both oxygen and propane on the surface of the catalyst.

4. Conclusions

In summary, the defect engineering method can be used to significantly improve the catalytic activities of the $LaCoO_3$ perovskite catalysts following the process of urea treatment. $LaCoO_3$-D43 exhibits the maximum catalytic activity (T_{90} = 309.3 °C). The recorded T_{90} was 150 °C lower than that of $LaCoO_3$. The maximum oxidation rate (15.33×10^{-6} mol g_{cat}^{-1} s^{-1}) and TOF (3.86×10^{-3} s^{-1}) were recorded at 225 °C. Excellent structural stability and thermal stability were achieved in the presence of 5 vol% of CO_2 and 5 vol% of H_2O. It has been demonstrated that the pyrolysis of urea increases the concentration of oxygen defects and results in the generation of perovskite octahedral distortions. This helps generate La defects. The process helps expose the surface-active Co species and oxygen vacancies present on the surface of

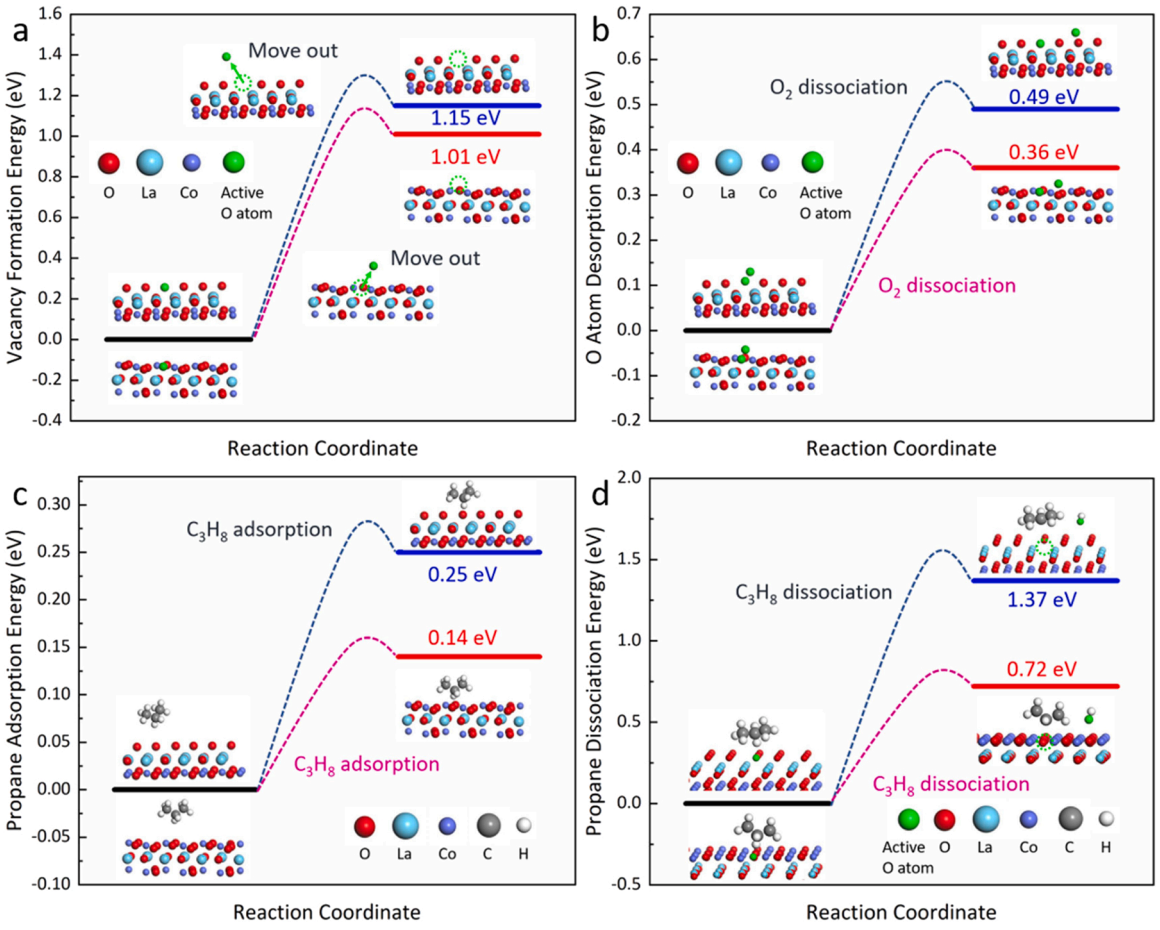

Fig. 9. (a) Vacancy formation energies, (b) O atom desorption energy, (c) propane adsorption energies, and (d) propane dissociation on La and the Co-exposed surface.

$LaCoO_3$, promoting the processes of adsorption, activation, and dissociation of the oxygen species and propane. This results in the increased extent of Co active site utilization. Analysis of the results obtained using the DFT technique also confirms that the Co-exposed surface characterized by high surface energy can facilitate the adsorption of O_2 and propane and help in the generation of active oxygen species and the dissociation of propane. This helps in significantly increasing the propane oxidation activity. All in all, our work proposed a defect engineering strategy to effectively activate and improve the performance of perovskite catalysts, that can also be generalized for the fabrication of other types of perovskite catalysts.

CRediT authorship contribution statement

Prof. **Yunqi Liu** conceived the idea; **Chao Feng** and **Qianqian Gao** synthesized the sample and performed most of the experiments; **Gaoyan Xiong** and **Yanfei Chen** participated in some characterization and/or reaction experiments; **Chao Feng** and Prof. **Yuan Pan** co-wrote the paper; Prof. **Zhaoyang Fei**, Prof. **Yanpeng Li**, Prof. **Yukun Lu** and Prof. **Chenguang Liu** provided the guidance of ideas and experiments. All authors discussed the results and commented on the manuscript.

Declaration of Competing Interest

The authors declare that they have no known competing financial interests or personal relationships that could have appeared to influence the work reported in this paper.

Acknowledgments

This work was financially supported by the National Natural Science Foundation of China (No. 21878334), the project sanctioned by the Chongqing Science and Technology Bureau (Grant no. cstc2019 jscx-gksb X0032), the projects sanctioned by the Chongqing Education Commission (Grant nos. KJZD-K201800801 and KJZD-M201900802), the State Key Laboratory of Materials-Oriented Chemical Engineering (KL20-09) and the Taishan Scholars Program of Shandong Province (No. tsqn201909065).

Notes

The authors declare no competing financial interest.

Appendix A. Supporting information

Supplementary data associated with this article can be found in the online version at doi:10.1016/j.apcatb.2021.121005.

References

[1] J.J. Kong, Z.W. Xiang, G.Y. Li, T.C. An, Introduce oxygen vacancies into CeO2 catalyst for enhanced coke resistance during photothermocatalytic oxidation of typical VOCs, Appl. Catal. B: Environ. 269 (2020), 118755.
[2] W.Z. Si, Y. Wang, S. Zhao, F.Y. Hu, J.H. Li, A facile method for in situ preparation of the MnO2/LaMnO3 catalyst for the removal of toluene, Environ. Sci. Technol. 50 (2016) 4572–4578.
[3] Y.F. Jian, M.J. Tian, C. He, J.C. Xiong, Z.Y. Jiang, H. Jin, L.R. Zheng, R. Albilali, J. W. Shi, Efficient propane low-temperature destruction by Co3O4 crystal facets

engineering: unveiling the decisive role of lattice and oxygen defects and surface acid-base pairs, Appl. Catal. B: Environ. 283 (2021), 119657.
[4] G.T. Chai, W.D. Zhang, L.F. Liotta, M.Q. Li, Y.L. Guo, A. Giroir-Fendler, Total oxidation of propane over Co3O4-based catalysts: elucidating the influence of Zr dopant, Appl. Catal. B: Environ. 298 (2021), 120606.
[5] Y. Liu, H. Zhou, R.R. Cao, X.Y. Liu, P.Y. Zhang, J.J. Zhan, L.F. Liu, Facile and green synthetic strategy of birnessite-type MnO2 with high efficiency for airborne benzene removal at low temperatures, Appl. Catal. B: Environ. 245 (2019) 569–582.
[6] Y.X. Jin, F.F. Li, P.X. Cui, Y. Yang, Q.P. Ke, M.N. Ha, W.C. Zhan, F. Ruan, C. Wan, Z. Lei, V.N. Nguyen, W. Chen, J. Tang, Jahn-Teller distortion assisted interstitial nitrogen engineering: enhanced oxygen dehydrogenation activity of N-doped MnxCo3−xO4 hierarchical micro-nano particles, Nano Res. 14 (2021) 2637–2643.
[7] M.S. Kamal, S.A. Razzak, M.M. Hossain, Catalytic oxidation of volatile organic compounds (VOCs) – a review, Atmos. Environ. 140 (2016) 117–134.
[8] Y. Wang, H. Arandiyan, H.A. Tahini, J. Scott, X. Tan, H.X. Dai, J.D. Gale, A.L. Rohl, S.C. Smith, R. Amal, The controlled disassembly of mesostructured perovskites as an avenue to fabricating high performance nanohybrid catalysts, Nat. Commun. 8 (2017) 15553.
[9] C.H. Zhang, C. Wang, S. Gil, A. Boreave, L. Retailleau, Y.L. Guo, J.L. Valverde, A. Giroir-Fendler, Catalytic oxidation of 1,2-dichloropropane over supported LaMnOx oxides catalysts, Appl. Catal. B: Environ. 201 (2017) 552–560.
[10] R.D. Zhang, P.X. Li, N. Liu, W.R. Yue, B.H. Chen, Effect of hard-template residues of the nanocasted mesoporous LaFeO3 with extremely high surface areas on catalytic behaviors for methyl chloride oxidation, J. Mater. Chem. A 2 (2014) 17329–17340.
[11] Y.B. Zheng, Y.Y. Chen, E.H. Wu, X.P. Liu, B.Q. Huang, H. Xue, C.L. Cao, Y.J. Luo, Q. R. Qian, Q.H. Chen, Amorphous boron dispersed in LaCoO3 with large oxygen vacancies for efficient catalytic propane oxidation, Chemistry 27 (2021) 4738–4745.
[12] J. Yang, L.M. Shi, L. Li, Y.R. Fang, C.Q. Pan, Y.H. Zhu, Z.F. Liang, S. Hoang, Z.G. Li, Y.B. Guo, Surface modification of macroporous La0.8Sr0.2CoO3 perovskite oxides integrated monolithic catalysts for improved propane oxidation, Catal. Today 376 (2021) 168–176.
[13] H. Li, J. Li, Z.H. Ai, F.L. Jia, L.Z. Zhang, Oxygen vacancy-mediated photocatalysis of BiOCl: reactivity, selectivity, and perspectives, Angew. Chem. Int. Ed. 57 (2018) 122–138.
[14] R.D. Zhang, W. Yang, J. Xue, B.H. Chen, The influence of O2, hydrocarbons, CO, H2, NOx, SO2, and water vapor molecules on soot combustion over LaCoO3 perovskite, Catal. Lett. 132 (2009) 10–15.
[15] R.D. Zhang, P.X. Li, R. Xiao, N. Liu, B. Chen, Insight into the mechanism of catalytic combustion of acrylonitrile over Cu-doped perovskites by an experimental and theoretical study, Appl. Catal. B: Environ. 196 (2016) 142–154.
[16] G. Kresse, D. Joubert, From ultrasoft pseudopotentials to the projector augmented-wave method, Phys. Rec. B 59 (1999) 1758–1775.
[17] Z. Liu, C. Chen, J.C. Zhao, L.Z. Yang, K.A. Sun, L.Y. Zeng, Y. Pan, Y.Q. Liu, C.G. Liu, Study on the NO2 production pathways and the role of NO2 in fast selective catalytic reduction DeNOx at low-temperature over MnOx/TiO2 catalyst, Chem. Eng. J. 379 (2020), 122288.
[18] C.M. Hou, W.C. Feng, L. Yuan, K.K. Huang, S. Feng, Crystal facet control of LaFeO3, LaCrO3, and La0.75Sr0.25MnO3, CrystEngComm 16 (2014).
[19] L. Yuan, K.K. Huang, S. Wang, C.M. Hou, X.F. Wu, B. Zou, S.H. Feng, Crystal shape tailoring in perovskite structure rare-earth ferrites REFeO3 (RE = La, Pr, Sm, Dy, Er, and Y) and shape-dependent magnetic properties of YFeO3, Cryst. Growth Des. 16 (2016) 6522–6530.
[20] X.Y. Wang, K.K. Huang, L. Yuan, S.B. Xi, W.S. Yan, Z.B. Geng, Y.G. Cong, Y. Sun, H. Tan, X.F. Wu, L.P. Li, S.H. Feng, Activation of surface oxygen sites in a cobalt-based perovskite model catalyst for CO oxidation, J. Phys. Chem. Lett. 9 (2018) 4146–4154.
[21] Y.T. Zhang, Q.W. Li, Y.J. Long, J.W. Zou, Z.L. Song, C. Liu, L.Y. Liu, F. Qi, B.B. Xu, Z.L. Chen, Catalytic ozonation benefit from the enhancement of electron transfer by the coupling of g-C3N4 and LaCoO3: discussion on catalyst fabrication and electron transfer pathway, Appl. Catal. B: Environ. 254 (2019) 569–579.
[22] E. Tamilalagan, A. Muthumariappan, T.W. Chen, S.M. Chen, S. Maheshwaran, P. J. Huang, A highly selective enzyme-free amperometric detection of glucose using perovskite-type lanthanum cobaltite (LaCoO3), J. Electrochem. Soc. 168 (2021), 086501.
[23] Y.P. Zhang, H.F. Liu, H.L. Hu, R.S. Xie, G.H. Ma, J.C. Huo, H.B. Wang, Orientation-dependent structural and photocatalytic properties of LaCoO3 epitaxial nano-thin films, Roy. Soc. Open Sci. 5 (2018), 171376.
[24] J.M. Jehng, I.E. Wachs, Structural chemistry and raman spectra of niobium oxides, Chem. Mater. 3 (1991) 100–107.
[25] T.Y. Zhang, C. Yang, S.L. Sun, Y.M. Huang, G. Meng, A.J. Han, J.F. Liu, Mesoporous Fe3O4@C nanoarrays as high-performance anode for rechargeable Ni/Fe battery, Sci. China Mater. 64 (2021) 1105–1113.
[26] M. Li, R.D. Zhang, H. Wang, H.X. Chen, Y. Wei, Role of the exposure facets upon diverse morphologies of cobalt spinels on catalytic deN2O process, Catal. Today 376 (2021) 177–187.
[27] H.S. Yu, X.J. Wei, J. Li, S.Q. Gu, The XAFS beamline of SSRF, Nucl. Sci. Tech. 26 (2015), 050102.
[28] X.Y. Wang, X.B. Peng, H.Y. Ran, B.Y. Lin, J. Ni, J.X. Lin, L.L. Jiang, Influence of Ru substitution on the properties of LaCoO3 catalysts for ammonia synthesis: XAFS and XPS studies, Ind. Eng. Chem. Res. 57 (2018) 17375–17383.
[29] X.Y. Wang, K.K. Huang, L. Yuan, S. Li, W. Ma, Z.Y. Liu, S.H. Feng, Molten salt flux synthesis, crystal facet design, characterization, electronic structure, and catalytic properties of perovskite cobaltite, ACS Appl. Mater. Interfaces 10 (2018) 28219–28231.
[30] X. Cheng, E. Fabbri, M. Nachtegaal, I.E. Castelli, M. El Kazzi, R. Haumont, N. Marzari, T.J. Schmidt, Oxygen evolution reaction on La1–xSrxCoO3 perovskites: a combined experimental and theoretical study of their structural, electronic, and electrochemical properties, Chem. Mater. 27 (2015) 7662–7672.
[31] T.A. Le, Y. Kim, H.W. Kim, S.U. Lee, J.R. Kim, T.W. Kim, Y.J. Lee, H.J. Chae, Ru-supported lanthania-ceria composite as an efficient catalyst for COx-free H2 production from ammonia decomposition, Appl. Catal. B: Environ. 285 (2021), 119831.
[32] L. Zhu, S.L. Chen, H. Zhang, J. Zhang, Y.W. Sun, X.M. Li, Z. Xu, L.F. Wang, J.R. Sun, P. Gao, W.L. Wang, X.D. Bai, Strain-inhibited electromigration of oxygen vacancies in LaCoO3, ACS Appl. Mater. Interfaces 11 (2019) 36800–36806.
[33] Q. Yu, C.X. Liu, X.Y. Li, C. Wang, X.X. Wang, H.J. Cao, M.C. Zhao, G.L. Wu, W. G. Su, T.T. Ma, J. Zhang, H.L. Bao, J.Q. Wang, B. Ding, M.X. He, Y. Yamauchi, X. S. Zhao, N-doping activated defective Co3O4 as an efficient catalyst for low-temperature methane oxidation, Appl. Catal. B: Environ. 269 (2020), 118757.
[34] Q.L. Shi, T.Z. Liu, Q. Li, Y. Xin, X.X. Lu, W.X. Tang, Z.L. Zhang, P.X. Gao, J. A. Anderson, Multiple strategies to decrease ignition temperature for soot combustion on ultrathin MnO2-x nanosheet array, Appl. Catal. B: Environ. 246 (2019) 312–321.
[35] P. Li, Y.N. Lin, S.E. Zhao, Y. Fu, W.Q. Li, R. Chen, S.H. Tian, Defect-engineered Co3O4 with porous multishelled hollow architecture enables boosted advanced oxidation processes, Appl. Catal. B: Environ. 298 (2021), 120596.
[36] M. Setvin, U. Aschauer, P. Scheiber, Y.F. Li, W.Y. Hou, M. Schmid, A. Selloni, U. Diebold, Reaction of O2 with subsurface oxygen vacancies on TiO2 anatase (101), Science 341 (2013) 988–991.
[37] H.F. Liu, B.G. Guo, K. Zheng, R.S. Xie, X.Q. Zhang, X.Y. Wu, Y.P. Zhang, C.B. Li, Novel visible-light-driven photoconductive properties of LaCoO3 epitaxial nano-thin films, Mater. Lett. 209 (2017) 446–449.
[38] H. Liu, W.L. Jia, X. Yu, X. Tang, X.H. Zeng, Y. Sun, T.Z. Lei, H.Y. Fang, T.Y. Li, L. Lin, Vitamin C-assisted synthesized Mn–Co oxides with improved oxygen vacancy concentration: boosting lattice oxygen activity for the air-oxidation of 5-(hydroxymethyl)furfural, ACS Catal. 11 (2021) 7828–7844.
[39] L.Q. Kang, B.L. Wang, Q.M. Bing, M. Zalibera, R. Büchel, R.Y. Xu, Q.M. Wang, Y. Y. Liu, D. Gianolio, C.C. Tang, E.K. Gibson, M. Danaie, C. Allen, K. Wu, S. Marlow, L.D. Sun, Q. He, S.L. Guan, A. Savitsky, J.J. Velasco-Vélez, J. Callison, C. Kay, S. E. Pratsinis, W. Lubitz, J.Y. Liu, F.R. Wang, Adsorption and activation of molecular oxygen over atomic copper(I/II) site on ceria, Nat. Commun. 11 (2020) 4008.
[40] H.L. Li, K. Yu, C. Wan, J.J. Zhu, X. Li, S. Tong, Y.X. Zhao, Comparison of the nickel addition patterns on the catalytic performances of LaCoO3 for low-temperature CO oxidation, Catal. Today 281 (2017) 534–541.
[41] S. Zhang, S.J. Liu, X.C. Zhu, Y. Yang, W.S. Hu, H.T. Zhao, R.Y. Qu, C.H. Zheng, X. Gao, Low temperature catalytic oxidation of propane over cobalt-cerium spinel oxides catalysts, Appl. Surf. Sci. 479 (2019) 1132–1140.
[42] Y.H. Wu, G.Y. Li, B.X. Chu, L.H. Dong, Z.F. Tong, H.X. He, L.L. Zhang, M.G. Fan, B. Li, L. Dong, NO reduction by CO over highly active and stable perovskite oxide catalysts La0.8Ce0.2M0.25Co0.75O3 (M = Cu, Mn, Fe): effect of the role in B site, Ind. Eng. Chem. Res. 57 (2018) 15670–15682.
[43] K.A. Sun, Y.Q. Liu, Y. Pan, H.Y. Zhu, J.C. Zhao, L.Y. Zeng, Z. Liu, C.G. Liu, Targeted bottom-up synthesis of 1T-phase MoS2 arrays with high electrocatalytic hydrogen evolution activity by simultaneous structure and morphology engineering, Nano Res. 11 (2018) 4368–4379.
[44] P.M. Shah, A.N. Day, T.E. Davies, D.J. Morgan, S.H. Taylor, Mechanochemical preparation of ceria-zirconia catalysts for the total oxidation of propane and naphthalene volatile organic compounds, Appl. Catal. B: Environ. 253 (2019) 331–340.
[45] Z.D. Huang, B. Xu, Z.G. Li, J.W. Ren, H. Mei, Z.N. Liu, D.G. Xie, H.B. Zhang, F.N. Dai, R.M. Wang, D.F. Sun, Accurately regulating the electronic structure of NixSey@NC core–shell nanohybrids through controllable selenization of a Ni-MOF for pH-universal hydrogen evolution reaction, Small, vol 16, 2020, 2004231.
[46] W.J. Yang, Y.F. Zhu, F. You, L. Yan, Y.J. Ma, C.Y. Lu, P.Q. Gao, Q. Hao, W.L. Li, Insights into the surface-defect dependence of molecular oxygen activation over birnessite-type MnO2, Appl. Catal. B: Environ. 233 (2018) 184–193.
[47] Z. Liu, G.X. Sun, C. Chen, K.A. Sun, L.Y. Zeng, L.Z. Yang, Y.J. Chen, W.H. Wang, B. Liu, Y.K. Lu, Y. Pan, Y.Q. Liu, C.G. Liu, Fe-doped Mn3O4 spinel nanoparticles with highly exposed Feoct–O–Mntet sites for efficient selective catalytic reduction (SCR) of NO with ammonia at low temperatures, ACS Catal. 10 (2020) 6803–6809.
[48] Y.L. Huang, C. Pellegrinelli, E.D. Wachsman, Oxygen dissociation kinetics of concurrent heterogeneous reactions on metal oxides, ACS Catal. 7 (2017) 5766–5772.
[49] P.F. Wang, J. Wang, X.W. An, J. Shi, W.F. Shangguan, X.G. Hao, G.W. Xu, B. Tang, A. Abudula, G.Q. Guan, Generation of abundant defects in Mn-Co mixed oxides by a facile agar-gel method for highly efficient catalysis of total toluene oxidation, Appl. Catal. B: Environ. 282 (2021), 119560.